

## HST Proper Motion of Andromeda III: Another Satellite Co-orbiting The M31 Satellite Plane

DANA I. CASETTI-DINESCU,<sup>1,2</sup> MARCEL S. PAWLOWSKI,<sup>3</sup> TERRENCE M. GIRARD,<sup>1</sup> KOSUKE JAMIE KANEHISA,<sup>3</sup>  
ALEXANDER PETROSKI,<sup>1</sup> MAX MARTONE,<sup>1</sup> VERA KOZHURINA-PLATAIS,<sup>4,5</sup> AND IMANTS PLATAIS<sup>6</sup>

<sup>1</sup>*Department of Physics, Southern Connecticut State University, 501 Crescent Street, New Haven, CT 06515, USA*

<sup>2</sup>*Astronomical Institute of the Romanian Academy, Cutitul de Argint 5, Sector 4, Bucharest, Romania*

<sup>3</sup>*Leibniz-Institut für Astrophysik (AIP), And der Sternwarte 16, D-14482 Potsdam, Germany*

<sup>4</sup>*Space Telescope Science Institute, 3700 San Martin Drive, Baltimore, MD 21218, USA*

<sup>5</sup>*Eureka Scientific, Inc., 2452 Delmer Street, Suite 100, Oakland, CA 94602-3017, USA*

<sup>6</sup>*Department of Physics and Astronomy, Johns Hopkins University, 3400 North Charles Street, Baltimore, MD 21218, USA*

Submitted to ApJ

### ABSTRACT

We measure the absolute proper motion of Andromeda III (And III) using ACS/WFC and WFPC2 exposures spanning an unprecedented 22-year time baseline. The WFPC2 exposures have been processed using a deep-learning centering procedure recently developed as well as an improved astrometric calibration of the camera. The absolute proper motion zero point is given by 98 galaxies and 16 *Gaia* EDR3 stars. The resulting proper motion is  $(\mu_\alpha, \mu_\delta) = (-10.5 \pm 12.5, 47.5 \pm 12.5) \mu\text{as yr}^{-1}$ . We perform an orbit analysis of And III using two estimates of M31's mass and proper motion. We find that And III's orbit is consistent with dynamical membership to the Great Plane of Andromeda system of satellites although with some looser alignment compared to the previous two satellites NGC 147 and NGC 185. And III is bound to M31 if M31's mass is  $M_{\text{vir}} \geq 1.5 \times 10^{12} M_\odot$ .

**Keywords:** Astrometry: Space astrometry — Proper motions: — Andromeda Galaxy: — Dwarf elliptical galaxies: — Local Group:

### 1. INTRODUCTION

Precision astrometry is revolutionizing our understanding of the local universe, all the way from exoplanets to the Milky Way and the Andromeda systems. Proper motions are the crucial measurements in deriving 3D velocities, which in turn open the access to a full dynamical analysis of a given system. Currently, this is only possible for the Milky Way galaxy and its satellite system, and for Andromeda (M31) and some of its satellites. Large distances to these systems imply very small tangential (angular) velocities which in turn require proper-motion uncertainties at the level of tens to a few of  $\mu\text{as yr}^{-1}$ .

Active effort in this direction requires primarily space-based observatories such as *HST*, *JWST* and *Gaia*. Unfortunately, *Gaia* cannot reach to the distances needed

for directly measuring faint systems at  $\sim 100$  kpc or more, at least not at the required precision for dynamical studies. On the other hand, *HST* and *JWST* are adequate platforms, provided time baselines in excess of 10 years are available. In which case *Gaia* can help to calibrate such *HST*-based studies, as we demonstrate in this study (see also Casetti-Dinescu et al. 2022; Bennet et al. 2023; Warfield et al. 2023).

Much like our own Milky Way system, the Andromeda system of satellites has about half of its satellites in a narrow plane referred to as the Great Plane of Andromeda (GPoA) (Conn et al. 2013; Savino et al. 2022). From line-of-sight velocities and the geometry of the plane, it is known that these satellites have a coherent motion suggesting a rotation in this plane (Ibata et al. 2013).

The origin and evolution of such thin, rotationally supported satellite configurations is currently unsettled; however, it is clear that these structures are not easily formed in state-of-the-art cosmological simulations, if at all. Taibi et al. (2024), for instance, discuss in detail the

Milky-Way system and highlight the astonishing degree of phase-space correlations for such in-plane satellites.

Regarding the M31 system, only two in-plane satellites have recently been measured by [Sohn et al. \(2020\)](#). Specifically, NGC 147 and NGC 185 were found to have proper motions consistent with co-rotation in this plane ([Sohn et al. 2020](#); [Pawlowski & Sohn 2021](#)).

In this paper we present the measurement of And III, a satellite situated on the southern side of M31, opposite NGC 147 and NGC 185, and only a little bit off the GPoA. Its line-of-sight velocity relative to M31 indicates And III is approaching us, while NGC 147 and NGC 185 are receding. We also present an orbit analysis of And III and argue in favor of its membership to the GPoA.

## 2. DATA SETS

Our proper-motion study is based on HST observations from three epochs, namely 1999, 2014 and 2021. The earliest epoch consists of WFPC2 exposures while the later ones are ACS/WFC exposures. All image data were downloaded from the Mikulski Archive for Space Telescopes (MAST). Details of these exposures are given in Table 1, including the original observing proposal id number (PID) for reference. All exposures are well-centered on And III, with relatively small offsets of between a few tenths of an arcsec to at most 3 arcsec. Astrometrically, the whole of the data set is of high value for two reasons: 1) the long time baseline of over 22 years lessens the impact of any residual, uncorrected positional errors (both systematic and random) within each detector, enhancing the true, proper-motion signal of our target, and 2) the existence of mid-epoch data serves as a useful tool for detecting any remaining systematic errors between the extreme-epoch data, as well as providing a check on spurious, outlier proper-motion values for individual stars.

In Figure 1 we illustrate the typical overlap between the earliest 1999 WFPC2 exposures and the later ACS/WFC exposures. The figure actually shows a 2014 ACS exposure, however, the 2021 ACS exposures were designed to align with the 2014 ones.

The center of And III, in equatorial coordinates, is adopted from [McConnachie \(2012\)](#). In Fig. 1 ( $\xi, \eta$ ) are the gnomonic projection of the equatorial coordinate system about this position. That is, the nominal center of And III is at  $(\xi, \eta) = (0, 0)$  in the figure.

## 3. DATA PROCESSING

### 3.1. WFPC2

The WFPC2 standard-calibrated `_c0m.fits` images from MAST are first corrected for cosmic-ray (CR) contamination. The purpose of the CR-cleaning is to

**Table 1.** Properties of the Data Sets

Camera	Epoch	Exposures	PID
WFPC2	1999.15	$16 \times 1300$ sec - F450W	7500
WFPC2	1999.15	$8 \times 1200$ sec - F555W	7500
ACS/WFC	2014.90	$11 \times 1264$ sec; $11 \times 1372$ sec - F475W	13739
ACS/WFC	2014.90	$11 \times 1086$ sec; $11 \times 1002$ sec - F814W	13739
ACS/WFC	2021.93	$7 \times 60$ sec; $14 \times 1118$ sec - F814W	16273

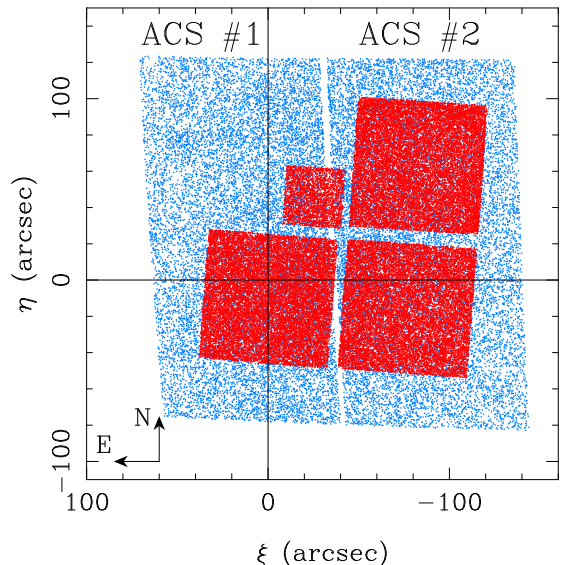


**Figure 1.** Overlap between the 1999 WFPC2 exposures (red symbols) and the modern 2014/2021 ACS/WFC exposures (blue symbols). Coordinates are a gnomonic projection of RA and DEC with the tangent point  $(\xi, \eta) = (0, 0)$  at And III's center ([McConnachie 2012](#)).

rectify the sky background statistics upon which the source-detection threshold depends, as well as to prevent the CRs themselves from being mistakenly detected as sources. Pairs of exposures with offsets less than 1 pixel are used to replace pixel values in the target image with those from the comparison image, when the difference in pixel values exceeds a given value-dependent level.

The CR-cleaned images are then processed for source detection and first-estimate centering using the classic *effective* PSF (ePSF) algorithm, i.e. the *hst1pass* code, 2023 version ([Anderson & King 2000](#); [Anderson 2022](#)). We note that WFPC2 ePSF libraries for filter F450W do not exist, thus we have used the F555W libraries for such images.

The next crucial step is refinement of the source  $(x, y)$  centers by application of the deep-learning (DL) model

recently developed by Casetti-Dinescu et al. (2024). This DL model was trained on a large set of WFPC2 exposures, also taken in 1999, at the core of globular cluster 47 Tuc. This latest DL model is an improvement over an earlier version (Casetti-Dinescu et al. 2023) in that it takes into account the PSF variation across the chip and as a function of magnitude. It has been developed for two filters, namely F555W and F814W. Here, we use the F555W model for both the F450W and F555W And III exposures.

It is worth emphasizing that WFPC2 images are severely undersampled and thus suffer from a fractional-pixel bias in the stars’ calculated centers, the result of any mismatch between the actual PSF and that assumed by the centering algorithm. In our experience, the standard *hst1pass* ePSF library for WFPC2 does not adequately remove this pixel-phase bias in many cases. The amplitude of the residual bias can as large as 40 to 50 mpix (Casetti-Dinescu et al. 2024). Unfortunately, once other astrometric corrections are applied, this bias is hard to detect as such, and essentially manifests itself as additional random noise in the stars’ centers. Our DL technique has proved to be successful on a number of other cluster targets (Casetti-Dinescu et al. 2024), therefore we choose to utilize it here. Here, we evaluated the impact of using DL centers versus *hst1pass* ones, utilizing the “bias curve” tool developed in Casetti-Dinescu et al. (2021), with which the distribution of the fractional pixel for all centers is compared to that of a uniform distribution (see e.g., Fig. 3 in Casetti-Dinescu et al. (2021)). The result, for these And III WFPC2 exposures, is that DL centering improves the residual bias, compared to *hst1pass* centering, by a factor of two, decreasing it roughly to the random noise level.

Once raw pixel positions are in hand, the following corrections are made: the well-known 34th-row correction (Anderson & King 1999), classic 3rd-order distortion correction (Anderson & King 2003), followed by the more recent higher-order distortion corrections mapped by Casetti-Dinescu et al. (2021). These distortion corrections were developed for filters other than F450W, thus, for the images in this filter, we have used the corrections for the closest-wavelength filter, namely F555W.

To assess the precision of the positions thus obtained, we perform a “plate” transformation between a reference exposure and a target exposure. The transformation is a classic polynomial one that includes up to 3rd-order terms (see e.g., Casetti-Dinescu et al. 2021), and the scatter of the residuals represents the errors in position of both the reference and the target image. Limiting the analysis to well-measured stars, we obtain single-

measurement standard errors of 44 mpix for the PC and 36 mpix for the WF chips, in filter F555W. This corresponds to 2 mas for the PC and 3.6 mas for the WF. These positional uncertainties are much larger than what we typically obtain for the WFPC2 camera in cluster fields, where we achieve errors of the order of 10 mpix (Casetti-Dinescu et al. 2024). The discrepancy is primarily attributable to an issue of signal-to-noise: the And III images we are measuring are predominantly faint stars that — in spite of the long exposure time — are in a lower signal-to-noise regime than the stars in more nearby globular clusters. In addition, CRs, although corrected for, may still affect the centering for a fraction of the stars. For filter F450W, positional errors are only a few percent larger than those for F555W, which is notable, considering the astrometric corrections we applied were developed for F555W.

### 3.2. ACS/WFC

For the ACS/WFC data, we work with `_flt.fits` files from MAST that have undergone the standard HST-pipeline calibration for bias, dark, and flat-field corrections. With these files, no charge transfer efficiency (CTE) correction has been applied to the image data. Rather, the CTE correction will be that implemented internally by *hst1pass*. CTE-corrected image data are available from MAST, i.e., `_flc`-type fits files, and we have performed centering tests using these files as well. For the short ACS exposures, (see Tab. 1), we find the `_flt` files provide slightly better positional precision, while for the long exposures, there is little difference in precision. Thus, we choose to use the `_flt` versions of the ACS data sets.

Once again, we use the 2023 version of the *hst1pass* code (Anderson 2022) to obtain positions and magnitudes of detected sources. Note that there are standard PSF library files and distortion corrections for both filters of ACS data sets being used here. The positions thus obtained have undergone all astrometric corrections implemented by *hst1pass*, including distortion and CTE correction. More specifically, the distortion is based on the work done in Kozhurina-Platais et al. (2015) and Kozhurina-Platais et al. (2018). Preliminary tests indicated that CR-correction did not significantly affect the performance of *hst1pass* detection or centering, for these data sets. Thus, we chose not to precorrect for CRs in the ACS images.

As in Sec. 3.1, we perform plate transformations for exposures taken at the same epoch and in the same filter to assess the positional precision. Long and short exposures are grouped separately. Single-measurement standard errors are calculated for well-measured stars.

For filter F814W we obtain  $\sim 15$  mpix in the long exposures and  $\sim 25$  mpix in the short exposures. The 2014- and 2021-epoch data have comparable errors. For filter F475W we obtain 24 mpix. These errors correspond to 0.75 mas, 1.25 mas, and 1.2 mas respectively. Comparing these values with the ones obtained for WFPC2 in Sec 3.1, it is clear that ACS/WFC positions are more precise. However, the time baseline of 22 years compared to 7 years with solely the ACS data renders the WFPC2 exposures quite competitive in the proper-motion determination. Also, the possibility of residual systematics inflating the final proper-motion errors, above that estimated from the random centering errors alone, argues for utilizing the longest time baseline available.

## 4. PROPER MOTIONS

### 4.1. Relative Proper Motions

Each chip of each camera is treated as a separate unit, i.e., each chip has its own, individual  $(x, y)$  system. Astrometrically corrected pixel coordinates, obtained in Secs. 3.1 and 3.2, are converted to equatorial coordinates,  $(\alpha, \delta)$ , using the linear WCS information in the header of the image fits files. Note that we do not depend on the WCS coefficients being very precise; they are not. Subsequent, higher-order transformations between chips will be made during the proper-motion reduction, overriding these approximate, low-order terms. However, working in a roughly common, equatorial system greatly facilitates star matching between the numerous images. Equatorial coordinates for all detections on each chip are then gnomonically projected into  $(\xi, \eta)$  standard coordinates assuming a uniform tangent point, which is taken to be the position of And III's center from McConnachie (2012), specifically  $(\alpha, \delta) = (8.89083, 36.49778)$  degrees.

Given the geometry of the various exposures' overlap (Fig. 1), we choose to construct two separate proper-motion catalogs, corresponding to the two ACS chips. As reference exposure, we adopt the initial 2014 F814W data set. The  $(\xi, \eta)$  positions from all other chips/exposures are transformed into either of the chips of this exposure, using polynomial transformations with up to 4th-order coefficients in each coordinate. The PC and WF2 chips of the WFPC2 are paired with ACS chip1, and WF3 and WF4 are paired with ACS chip2. An iterative least-squares procedure is employed to refine both the polynomial coefficients of each chip/exposure into the reference exposure, and every object's proper motion; the initial iteration assumes zero proper motions for all reference stars. The reference stars that are used to perform the transformations and

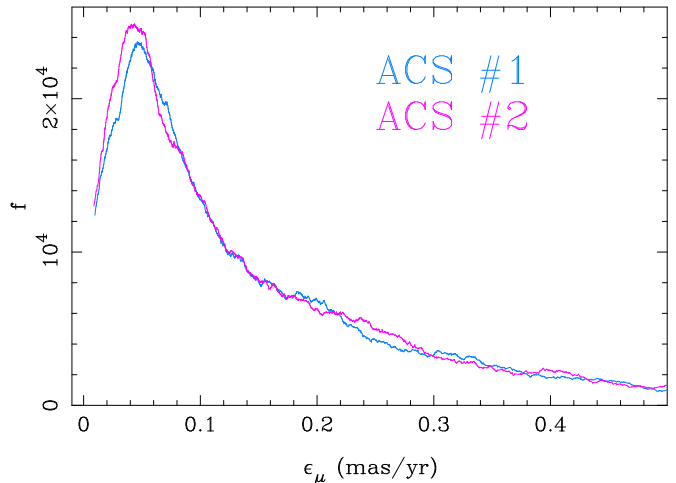


**Figure 2.** Distribution of formal proper-motion uncertainties in the two catalogs, corresponding to each ACS chip. Here we show uncertainties in  $\mu_\alpha$ ; we obtain a similar distribution for  $\mu_\delta$ .

compute the polynomial coefficients are predominantly And III stars. The proper-motion system is thus relative, and since the reference stars are dominated by And III members, the system is roughly that of And III.

We calculate proper motions<sup>1</sup> for all objects that have a minimum of 10 separate position measurements and a minimum of 7 years time baseline. Proper motions are the slope of simple linear fits to each coordinate as a function of time, removing the highest outlier if it deviates more than  $2.5\sigma$  from the best-fit line, until no such outliers remain. Formal relative proper-motion uncertainties are calculated from the scatter about this best-fit line.

In this manner, two **independent** relative proper-motion catalogs are constructed, one for each of the two ACS chips. The distribution of formal, random proper-motion uncertainties in each catalog is shown in Figure 2. The uncertainty distributions peak at  $\sim 40 \mu\text{as yr}^{-1}$ .

As one would expect, proper-motion uncertainties increase with magnitude, as illustrated in Figure 3. Here, as an example, we show the proper-motion uncertainty in  $\mu_\alpha$  as a function of F814W instrumental magnitude for the ACS chip-1 catalog. (Similar looking plots are obtained for  $\mu_\delta$  and for ACS chip 2.) Stars with baselines of 7 years (ACS only) and 22 years (WFPC2 and ACS) are highlighted. There are very few stars with a baseline of 15 years, (i.e., missing ACS measures in 2021). Formal proper-motion uncertainties of the best-

<sup>1</sup> Throughout the paper,  $\mu_\alpha$  is actually  $\mu_\alpha \cos \delta$ , and as units for the proper motions we will use both  $\text{mas yr}^{-1}$  and  $\mu\text{as yr}^{-1}$ .



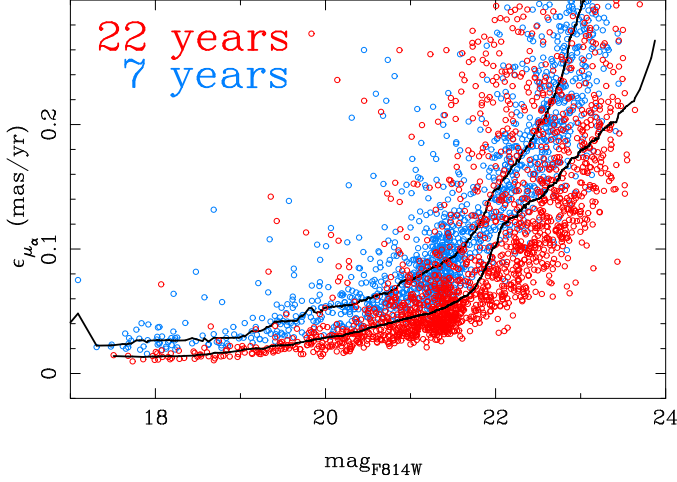


**Figure 3.** Formal proper-motion uncertainty as a function of instrumental magnitude in F814W for the ACS chip-1 catalog. Two groups are highlighted: stars that have a 7- and a 22-year baseline. A moving median is represented with a black line for each sample. For reference, the horizontal branch of And III is at  $\text{mag}_{F814W} \sim 21.4$ , where a higher stellar density is apparent.

measured stars are of the order of  $\sim 18 \mu\text{as yr}^{-1}$  for the 22-year sample. These remain tightly distributed around a median value out to  $\text{mag}_{F814W} \sim 22$ . Fainter than this value, the uncertainties continue to increase in value and in scatter. The 7-year sample, based on ACS data only, has best-measured uncertainties of  $\sim 25 \mu\text{as yr}^{-1}$  and exhibit a larger scatter compared to the 22-year sample. Toward faint magnitudes the 7-year uncertainties increase, but with less scatter than that of the 22-year sample.

#### 4.2. Correction to Absolute Proper Motions

We use *Gaia* Early Data Release 3 (EDR3) (*Gaia Collaboration et al. 2021*) stars and background galaxies to establish the correction to absolute proper motion for our catalogs. Values for these two types of correction are derived separately and later combined, by weighted average, to achieve our final correction to absolute. It will be seen that the EDR3 correction is significantly less certain than that based on galaxies, and contributes to the final value at a roughly 10 percent level. Nonetheless, this correction anchors the bright end of our stellar proper motions and is deemed an important check on the galaxies which anchor the faint end. Furthermore, future *Gaia* Data Releases will improve the proper-motion precision at the faint end. For example, it is expected that *Gaia* DR4 based on 66 months of observations (compared to 34 months in EDR3) will improve precision by more than a factor of two. Thus the *Gaia*-based absolute correction can be re-addressed once future releases are made available.

##### 4.2.1. EDR3-based correction

EDR3 stars that appear in our catalogs are at the faint end of *Gaia*'s reach and at the bright end of our study. As such, EDR3 proper-motion errors will dominate the error budget in the differences. It is worth noting that these EDR3 stars are Galactic foreground stars and therefore will have substantial proper motions. Crucial to being able to include these stars are the short ACS exposures taken in 2021 (see Tab. 1).

For the ACS chip-1 catalog we identify 8 EDR3 stars: all with *Gaia*  $G$  magnitudes between 17.1 and 20.8, except for one star at  $G = 13.3$ . This latter star was effectively too bright for our study and thus we discard it from consideration. The remaining 7 EDR3 stars have EDR3 proper-motion uncertainties ranging from 0.06 to  $1.16 \text{ mas yr}^{-1}$ , while our proper-motion uncertainty estimates range from 0.02 to  $0.16 \text{ mas yr}^{-1}$ . For the ACS chip-2 catalog, we identify 10 EDR3 stars. Again we eliminate the brightest one at  $G = 16.5$  which was poorly measured in our catalog as being near saturation. The remaining 9 EDR3 stars have  $G$  magnitudes between 17.3 and 20.9. Their EDR3 proper-motion uncertainties range between 0.06 and  $1.46 \text{ mas yr}^{-1}$ , while our catalog uncertainties range between 0.01 and  $0.18 \text{ mas yr}^{-1}$ . All 16 EDR3 stars have Renormalized Unit Weight Error values between 0.93 and 1.04, and are thus in the nominal range for single sources. In our system of F814W instrumental magnitudes, the EDR3 stars fall between  $\text{mag}_{F814W} = 13$  and 17.

We compute proper-motion differences between our relative proper motions and EDR3 absolute ones. The weighted mean of these differences is used to determine the EDR3-based correction to absolute proper motion for each catalog. The weights are taken to be the quadrature sum of the EDR3 proper-motion uncertainties and those from our catalogs<sup>2</sup>. The weighted-mean values are presented in Table 2 for the two catalogs, i.e., ACS chips. Even though the uncertainties of the EDR3-based correction are somewhat large, it is apparent that the correction is near zero in  $\mu_\alpha$  while it significantly departs from zero in  $\mu_\delta$ . In Figure 4, left panel we show the distribution of these proper-motion differences, where

<sup>2</sup> An effort has been made to estimate the amplitude of possible systematic errors for these bright stars in our sample. Examining proper-motion trends with magnitude and extrapolating to these stars' regime, tentative corrections in each field and along each axis vary but are only marginally significant. Even the largest of these has well under a 1-sigma effect on our final combined zero-point correction, while the final combined estimated uncertainties remain unchanged. For this reason, we choose not to attempt to include them.

the error bars are the combined 1-sigma uncertainties, from EDR3 and our catalogs.

#### 4.2.2. Galaxies-based correction

The 2014 F814W set of 22 exposures is used to identify background galaxies in our two catalogs. Each of these is CR-cleaned using the same procedure as in Sec. 3.1 for the WFPC2 images. The ACS images are then shifted to align with the first one in the set and median-combined to form a single, deep image. This median image is searched by eye for galaxies. In the chip-1 catalog we initially identify 65 galaxies, while in the chip-2 catalog we have 83 galaxies with computed relative proper motions. We then discard all galaxies with combined proper-motion uncertainty  $\sqrt{(\epsilon_{\mu_\alpha}^2 + \epsilon_{\mu_\delta}^2)} > 1.0$

mas yr<sup>-1</sup>. Galaxies with large proper motions (more than  $3\sigma$  from the mean) are also discarded. We are thus left with 46 galaxies in the ACS chip-1 catalog, and 52 galaxies in the ACS chip-2 catalog.

Our measures for the relative proper motions of these galaxies are shown in Fig. 4, middle panel. We calculate once again a weighted mean proper motion of the galaxies, where the weights are given by the proper-motion errors. These galaxy-based corrections to absolute proper motions are also listed in Tab. 2 and are to be directly compared with the EDR3-based values in the same Table. It is reassuring that the galaxy-based corrections also indicate a value near zero in  $\mu_\alpha$  while showing a significant departure from zero in  $\mu_\delta$  and in the same negative direction as the EDR3 correction. The weighted averages for both galaxies and EDR3 correction are shown in the right panel of Fig. 4.

**Table 2.** Corrections to Absolute Proper Motion from EDR3 stars and galaxies

Cat.	$N_{EDR3}$	$\mu_\alpha^{EDR3}$	$\mu_\delta^{EDR3}$	$N_{Gal}$	$\mu_\alpha^{Gal}$	$\mu_\delta^{Gal}$
		(mas yr <sup>-1</sup> )	(mas yr <sup>-1</sup> )		(mas yr <sup>-1</sup> )	(mas yr <sup>-1</sup> )
#1	7	$-0.009 \pm 0.087$	$-0.154 \pm 0.062$	46	$-0.006 \pm 0.021$	$-0.051 \pm 0.022$
#2	9	$0.015 \pm 0.069$	$-0.100 \pm 0.056$	52	$0.018 \pm 0.013$	$-0.022 \pm 0.015$

## 5. AND III'S ABSOLUTE PROPER MOTION

Finally, to determine the systemic, absolute proper motion of And III one must compute the average relative motion of And III stars and subtract from it the correction to absolute proper motion. Our adopted correction to absolute is a weighted mean of the two values in Tab. 2, i.e., the EDR3- and galaxy-based corrections. The final adopted corrections are listed in Table 3, columns 2 and 3.

The vast majority of stars in our sample are members of And III and, as such, can be used to calculate its systemic, relative motion. We use stars with  $\text{mag}_{F814W}$  between 17 and 24, with combined proper-motion uncertainties  $\leq 0.5$  mas yr<sup>-1</sup>, and with total proper motion  $\leq 0.5$  mas yr<sup>-1</sup>. The mean and its uncertainty are computed using probability plots (Hamaker 1978) with trimming of the extreme 10% of both wings to eliminate the influence of potential outliers. The method essentially fits the inner 80% of the distribution to a shifted and scaled Gaussian to determine the mean and uncertainty. We choose to use this mean and not one weighted by the proper-motion uncertainties, as the latter leads to an unrealistically small uncertainty in the weighted mean, of the order of  $1 \mu\text{as yr}^{-1}$ .

In the chip-1 catalog there are 2396 stars participating in the mean, and in the chip-2 catalog there are 2176 stars. The mean relative proper motion in each catalog is listed in Table 3, columns 4 and 5.

Note that we have also performed a mean relative motion based on And III members selected via the satellite's sequence in the color-magnitude diagram (CMD). For this purpose a CMD was constructed from the 2014 data set. Instrumental magnitudes in F814W and F475W are obtained as averages of individual object measurements in each exposure. Each exposure is placed on the “system” of the first exposure in the 2014 data set by determining offsets between the magnitudes in the reference exposure and the target one. The CMD-based mean proper motion agrees within errors to the magnitude-only trimmed star sample. This confirms that, in the magnitude range we considered, the stars in our field are predominantly And III members. Furthermore, tests demonstrate that the derived mean motion is *not* sensitive to the faint-magnitude limit adopted.

In Figure 5 we show the characteristics of our two proper-motion catalogs, for stars with proper-motion errors  $\leq 0.5$  mas yr<sup>-1</sup>. The upper-left panel shows the spatial distribution of stars, where the oval shape of the

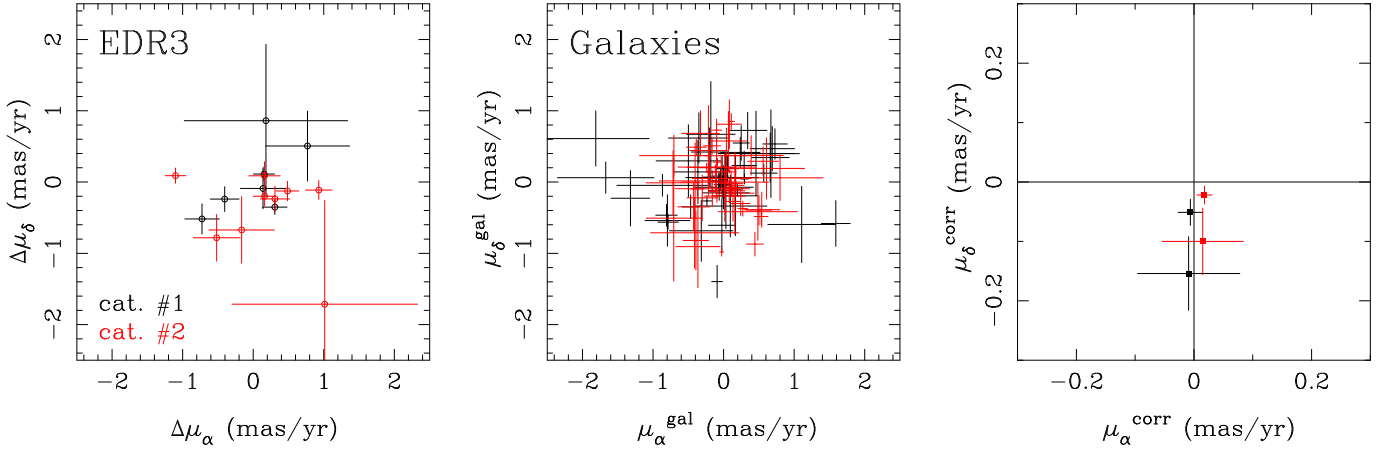


**Figure 4.** Correction to absolute proper motions as given by EDR3 stars (left panel) and galaxies (middle panel); each of the two ACS chip catalogs is as indicated. The right panel shows the weighted averages as computed in Tab. 2. The symbols with large error bars in this panel correspond to the EDR3-based values. Note the difference in scale between the first two panels and the right-most one.

galaxy is apparent in the stellar density. Here, we also display the vector of the proper motion of And III with respect to M31, and its cone of uncertainty. For M31, we used the weighted average with the EDR3 proper motion from Pawlowski & Sohn (2021) as detailed in Sec. 6.1. It appears that this motion is aligned with the elongation of And III. The upper-right panel in Fig. 5 shows the relative proper motion distribution, followed by the run of proper motions with magnitude in the middle panels. The concentration of stars at magnitude  $\sim 21.5$  is the horizontal branch of And III. Finally, we present the instrumental CMD obtained from the 2014 data, for stars with proper-motion uncertainties  $\leq 0.5$  mas yr $^{-1}$ , showing that the dominant stellar population is that of And III.

Finally, we note that a line-of-sight velocity membership selection was made using data from Kirby et al. (2020). In the ACS chip-1 catalog there were 13 stars with measured line-of-sight velocities, while in the chip-2 catalog there was only one star. These stars are very near the bright limit of our catalogs: F814W instrumental mag = 17.6 - 19.3. Therefore we fear that residual CTE is likely to affect the mean proper motion at a level larger than the formal errors, for so few stars. Thus, we have decided not to make use of this membership information.

The absolute proper-motion values obtained independently per each ACS chip are listed in the last two columns of Tab. 3. Finally, the adopted absolute proper motion of And III is taken to be the straight average of the two determinations, with the uncertainty estimated from the difference of these values. We believe the scatter (albeit only two determinations) is a better real-world assessment of the uncertainty of our final measurement as residual systematic errors are prob-

ably present at this level. Our final value for the absolute proper motion of And III is thus  $(\mu_\alpha, \mu_\delta) = (-10.5 \pm 12.5, 47.5 \pm 12.5)$   $\mu\text{as yr}^{-1}$ .

## 6. ORBIT ANALYSIS

### 6.1. Orbital Properties and Constraints on M31's Mass

We calculate the space position and velocity of And III by combining our derived proper motion with other observed parameters. Namely, we use RR Lyrae-based heliocentric distances for M31 ( $776.2^{+22}_{-21}$  kpc) and And III ( $721.1^{+17}_{-16}$  kpc) by Savino et al. (2022), along with radial velocities of  $-300.1 \pm 3.9$  km s $^{-1}$  and  $-344.3 \pm 1.7$  km s $^{-1}$  (McConnachie 2012), respectively. In particular, the value we adopt for M31's proper motion strongly influences the resulting kinematics of And III. We therefore test two PM estimates: the fiducial HST+Sats value used in Sohn et al. (2020)  $(\mu_\alpha, \mu_\delta) = (34.3 \pm 8.4, -20.2 \pm 7.8)$   $\mu\text{as yr}^{-1}$ , as well as its weighted average with the EDR3 proper motion by Salomon et al. (2021). The latter  $(\mu_\alpha, \mu_\delta) = (40.1 \pm 6.6, -28.3 \pm 5.6)$   $\mu\text{as yr}^{-1}$  calculated in Pawlowski & Sohn (2021) arguably represents our current best estimate of M31's systemic proper motion.

To describe the space positions and velocities for And III, we adopt the M31-centric coordinate system as follows. Observed parameters are first transformed into a Cartesian Galactocentric frame, then translated into M31's rest frame. Finally, we apply a rotation such that the X-Y plane is aligned with M31's galactic disc, while the X-axis points away from the Milky Way's direction. This is functionally equivalent to the frame adopted in Sohn et al. (2020), although we instead adopt updated distances from Savino et al. (2022). Observational errors are accounted for by propagating uncertainties for

**Table 3.** And III: Relative and Absolute Proper Motion

Cat.	$\mu_{\alpha}^{cor}$ (mas yr <sup>-1</sup> )	$\mu_{\delta}^{cor}$ (mas yr <sup>-1</sup> )	$\mu_{\alpha}^{rel}$ (mas yr <sup>-1</sup> )	$\mu_{\delta}^{rel}$ (mas yr <sup>-1</sup> )	$\mu_{\delta}^{abs}$ (mas yr <sup>-1</sup> )	$\mu_{\delta}^{abs}$ (mas yr <sup>-1</sup> )
#1	$-0.006 \pm 0.020$	$-0.063 \pm 0.021$	$-0.004 \pm 0.004$	$-0.003 \pm 0.003$	$0.002 \pm 0.020$	$0.060 \pm 0.021$
#2	$0.018 \pm 0.013$	$-0.027 \pm 0.014$	$-0.005 \pm 0.005$	$0.008 \pm 0.004$	$-0.023 \pm 0.014$	$0.035 \pm 0.015$

**Table 4.** Orbital parameters.

M31 PM	$M_{vir,M31}$ ( $\times 10^{12} M_{\odot}$ )	$f_{peri}^a$ (%)	$t_{peri}^b$ (Gyr)	$r_{peri}^c$ (kpc)	$f_{apo}^a$ (%)	$t_{apo}^b$ (Gyr)	$r_{apo}^c$ (kpc)	$e^d$
HST+sats	1.5	29	– [2.4, 5.2]	– [49, 84]	52	4.6 [1.5, 4.6]	490 [184, 483]	0.70 [0.57, 0.86]
”	2.0	54	4.9 [2.2, 5.0]	76 [49, 89]	78	2.4 [1.1, 3.9]	305 [164, 474]	0.60 [0.50, 0.80]
HST+sats+EDR3	1.5	11	– [3.3, 5.6]	– [53, 86]	28	– [2.0, 4.8]	– [245, 508]	0.83 [0.68, 0.89]
”	2.0	31	– [2.8, 5.3]	– [49, 86]	57	4.4 [1.7, 4.5]	525 [217, 533]	0.72 [0.60, 0.85]

NOTE—Orbital parameters of And III after integrating backward for 6 Gyr. Uncertainties are included as [15.9, 84.1] percentiles. Parameters denoted with a dash represent cases lacking a last pericentric or apocentric passage within the last 6 Gyr.

<sup>a</sup>Fraction of orbits that achieved peri/apocentric passage over the last 6 Gyr.

<sup>b</sup>Lookback time to last peri/apocentric passage.

<sup>c</sup>Distance from M31 at the last peri/apocentric passage.

<sup>d</sup>Eccentricity of the orbit.

distances, radial velocities and proper motions for both And III and M31 in a Monte Carlo fashion. We thus generate 100 initial conditions for backward integration alongside the most likely observed parameters.

To perform orbit integrations, we adopt two mass models for M31’s potential from Table 2 of [Patel et al. \(2017\)](#) – a higher-mass M31 with a virial mass of  $M_{vir} = 2 \times 10^{12} M_{\odot}$  and a lower-mass M31 with  $M_{vir} = 1.5 \times 10^{12} M_{\odot}$ . In addition, both potentials also contain a central Hernquist bulge and Miyamoto-Nagai disc to represent the baryonic galaxy. Since we lack internal kinematics for And III, we estimate the effects of Chandrasekhar dynamical friction for a Plummer sphere with  $M = 10^{10} M_{\odot}$  and  $R = 1$  kpc, a model close to that adopted for NGC 185 in [Sohn et al. \(2020\)](#). The strength of the dynamical friction implemented thus serves as an upper bound (although we find modifying this component does not have a large impact on the resulting orbits).

We integrate And III and its Monte Carlo realizations backward for a period of 6 Gyr with M31’s position fixed throughout. Due to the individual error contributions in distance and proper motion for both And III and M31

especially, analytic orbits show a large scatter in their orbital properties (Table 4). In all realizations, And III is currently approaching pericenter and will perform its closest approach within the next 0.5 Gyr following a moderately eccentric orbit ( $\langle e \rangle = 0.6 - 0.83$ ). Whether And III is bound or on first infall is uncertain and depends heavily on the adopted M31 mass and choice of proper motion. Due to the direction of M31’s motion enhancing the fly-by velocity of And III, the EDR3 PM weighted average generally requires a more massive M31 potential to keep And III bound compared to HST+Sats alone. We note that And III in the higher-mass M31 potential with the EDR3-based proper motion for M31 follows a very similar orbit as in the lower-mass potential with HST+Sats, with its last apocenter around 4.5 Gyr ago. If on first infall, And III would have been accreted from the far side of M31 and will spend a majority of its orbit there, marking its participation in M31’s global asymmetric distribution of satellites towards the Milky Way ([Savino et al. 2022](#)) a purely transient event.

Due to its higher M31-centric velocity compared to NGC 147 and NGC 185, the kinematics of And III serves as a useful probe to constrain the virial mass of M31 un-



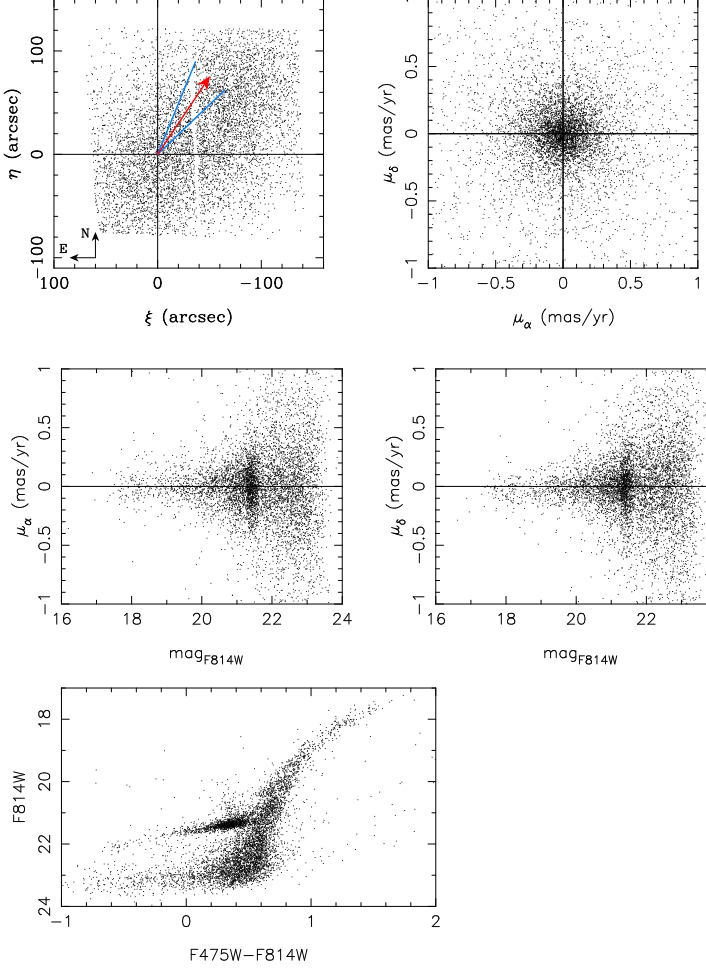


**Figure 5.** Spatial distribution, proper motions and CMD of our two catalogs, for stars with proper-motion uncertainties  $\leq 0.5 \text{ mas yr}^{-1}$ . The vector in the first panel marks the proper motion of And III with respect to M31 and its cone of uncertainty. M31’s proper motion is the weighted average with the EDR3 proper motion from [Pawlowski & Sohn \(2021\)](#), see also Sec. 6.1.

der the assumption that it is bound to M31, not on first infall. In this case, the satellite’s total velocity  $v_{\text{tot}}$  in the host’s rest frame must not exceed the escape velocity  $v_{\text{esc}} = \sqrt{-2\phi(r)}$  (where  $\phi(r)$  is the gravitational potential of the halo and any baryonic galaxy component), thus setting a lower bound on the permissible host mass. In Fig. 7, we compare the total velocity of And III to the escape velocities at each radius from our two adopted mass models for M31 ([Patel et al. 2017](#)). For both M31 proper motions, And III appears to be bound to M31 at  $M_{\text{vir}} \geq 1.5 \times 10^{12} M_{\odot}$ . And III is fully above the  $v_{\text{esc}}$  curve if M31 were to have a similar halo mass as the Milky Way, which effectively constrains M31’s potential to be more massive than our Galaxy’s, if And III is gravitationally bound.

## 6.2. Alignment with to GPoA

As discussed earlier, And III previously has been identified as a member of the Great Plane of Andromeda. It’s spectroscopic systemic velocity follows the dominant line-of-sight velocity trend indicative of a co-rotating satellite plane. Two other on-plane satellite galaxies for which proper motions have been measured, NGC 147 and NGC 185, have both been found to be consistent with co-orbiting along this plane ([Pawlowski & Sohn 2021](#)). In Figure 8 we show the on-sky distribution of M31’s satellites with the velocity vectors of the three satellites with measured proper motions highlighted. Here, we repeat the analysis in [Pawlowski & Sohn \(2021\)](#) for And III.

Among satellites of M31, And III is the one most offset the GPoA (Fig. 8) that is still considered a member of this structure. Its most-likely spatial position already places it at an offset of  $21.5^\circ$  from the satellite plane. This implies that its orbital pole can not align to better than this angle with the normal to the satellite plane, for which we adopt  $(l, b) = (205.8^\circ, 7.6^\circ)$  following [Pawlowski & Sohn \(2021\)](#).

As before, we consider two possible proper motions for M31. We then sample  $10^5$  Monte-Carlo realizations varying the positions, proper motions, and line-of-sight velocities of M31 and the satellite within their uncertainties. For each realization we measure the position of the orbital pole of And III relative to M31, and its angle to the GPoA normal vector. The resulting distribution of orbital pole directions is shown in Fig. 9. The distribution of alignment angles, in comparison to those inferred for NGC 147 and NGC 185, is shown in Fig. 10. Both figures are based on assuming the “HST+Sats+EDR3” proper motion for M31 (the plots look visually very similar if adopting the “HST+Sats” instead).

For the “HST+Sats” proper motion, we find that the peak of the orbital pole uncertainty cloud points to  $(l, b) = (234.8^\circ, 30.0^\circ)$  and is  $35.3^\circ$  from the GPoA normal, while the median offset of all realizations is  $41.6^\circ$  and has a standard deviation of  $14.7^\circ$ . The one (two)  $\sigma$  spread in this alignment angle is  $30.4^\circ$  to  $56.7^\circ$  ( $21.3^\circ$  to  $81.8^\circ$ ). Using only the most-likely values in all measured parameters, we find that the most-likely orbital pole points to  $(l, b) = (241.2^\circ, 31.0^\circ)$  and has an angular offset from the GPoA normal vector of  $40.5^\circ$ .

The alignment is slightly worse if we instead adopt the “HST+Sats+EDR3” proper motion. The orbital pole peak now points to  $(l, b) = (237.7^\circ, 32.8^\circ)$ ,  $38.8^\circ$  from the GPoA normal. The median offset is  $42.1^\circ$  with a standard deviation of  $14.4^\circ$ , while the one (two)  $\sigma$  spread is  $31.9^\circ$  to  $57.1^\circ$  ( $23.5^\circ$  to  $82.6^\circ$ ). The most-likely orbital

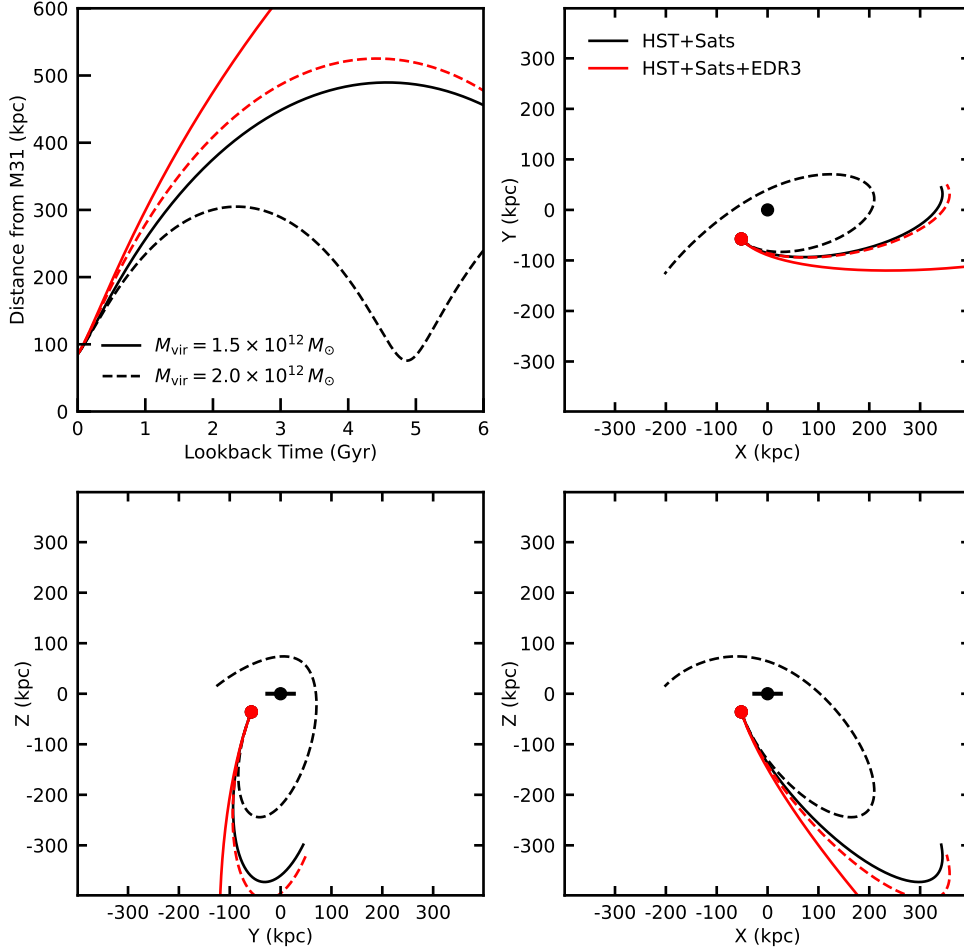


**Figure 6.** Backward orbit integrations of And III around M31 over the last 6 Gyr for a low-mass ( $M_{\text{vir}} = 1.5 \times 10^{12} M_{\odot}$ ) and high-mass ( $M_{\text{vir}} = 2 \times 10^{12} M_{\odot}$ ) M31 model, in solid and dashed lines, respectively. The black orbits adopt the HST+Sats M31 proper motion, while the red orbits assume a weighted average with M31’s EDR3 proper motion. Andromeda’s disc lies along the X-Y plane, while the Milky Way lies along the negative X-axis.

pole points to  $(l, b) = (241.8^{\circ}, 31.8^{\circ})$ , which implies an angular offset of  $41.3^{\circ}$  from the GPoA normal.

Within the measurement uncertainties, And III appears to be consistent with co-orbiting along the GPoA to within the geometrically allowed limit. Its orbit is likely less well aligned than those of other two M31 satellites with measured proper motions, which are both consistent with a perfect orbital alignment, but Fig. 10 shows considerable overlap in the distribution of possible orbital alignment angles of all three satellites, within a range comparable to the typically considered orbital pole alignment angle for the Milky Way satellite galaxies of  $37^{\circ}$  (see e.g. Taibi et al. 2024). However, among the objects considered to make up the M31 satellite plane, And III is the most spatially offset. As such, it could well have turned out to show an entirely unaligned orbit, or even one that is counter-orbiting (despite its agreement with the line-of-sight velocity trend, see its possible range of proper motions in Figure 11 of Pawlowski

& Sohn 2021). This suggests that And III is indeed associated with the M31 satellite plane, though improved accuracy in the measured proper motion is required to firmly establish this.

## 7. SUMMARY

We have measured the absolute proper motion of And III using ACS and WFPC2 exposures over three epochs and spanning up to 22 years. Novel astrometric techniques have been used to process the WFPC2 images. The spatial location of And III is some  $20^{\circ}$  offset from the GPoA satellite plane. Nevertheless, based on the line-of-sight velocity and proximity to this plane, And III is considered a member of this plane. The proper-motion measurement enables an orbit analysis that favors dynamical membership to this structure. If And III is bound to M31, then it implies an M31 mass  $M_{\text{vir}} \geq 1.5 \times 10^{12} M_{\odot}$ , larger than that of the Milky Way.

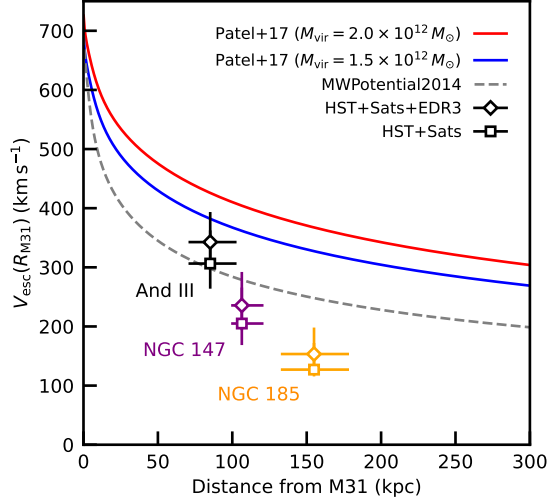


**Figure 7.** The M31-centric distance and total velocity of And III (black) using the HST+sats M31 proper motion (square) and its weighted average with EDR3 (diamond). Escape velocity curves of the two M31 mass models adopted in this paper are shown in blue and red, while a Milky Way-like potential is displayed for reference (grey dashed line). Results for NGC 147 and NGC 185, two other M31 satellites with proper motions, are also shown in purple and orange respectively.

We also find that the motion of And III with respect to M31 is aligned with the long axis of the satellite.

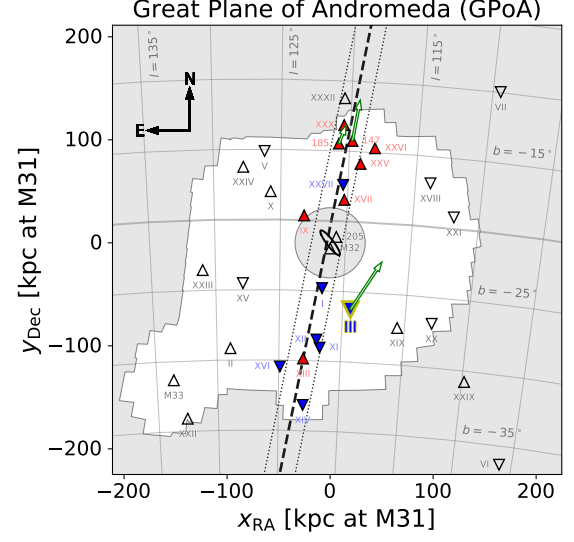


**Figure 8.** Spatial distribution of satellite galaxies around M31. Upward/downward triangles mark those satellites with receding/approaching line-of-sight velocities relative to that of M31. Filled symbols mark the candidate members of the GPoA according to their line-of-sight velocities and spatial distribution, with red/blue color also indicating the receding/approaching satellites. The GPoA and its estimated width are highlighted with dashed and dotted lines, respectively. The on-sky velocities relative to that of M31 for NGC 147, NGC 185 (Sohn et al. 2020) and And III (this work) are marked with green arrows.

## ACKNOWLEDGMENTS

This work was supported by program HST-AR-17029 provided by NASA through a grant from Space Telescope Science Institute, which is operated by the Association of Universities for Research in Astronomy, Inc. MSP acknowledges funding via a Leibniz-Junior Research Group (project number J94/2020).

This study has made use of data from the European Space Agency (ESA) mission *Gaia* (<https://www.cosmos.esa.int/gaia>), processed by the Gaia Data Processing and Analysis Consortium (DPAC, <https://www.cosmos.esa.int/web/gaia/dpac/consortium>). Funding for the DPAC has been provided by national institutions, in particular the institutions participating in the *Gaia* Multilateral Agreement.

All the *HST* data sets used in this paper can be found in MAST. Set 1 corresponds to all WFPC2 observations, while Set 2 to all ACS observations.

Set 1: <http://dx.doi.org/10.17909/r78a-kn48>

Set 2: <http://dx.doi.org/10.17909/62eg-0f60>

Orbital pole of AndIII assuming HST + Sat + GaiaEDR3 proper motion for M31

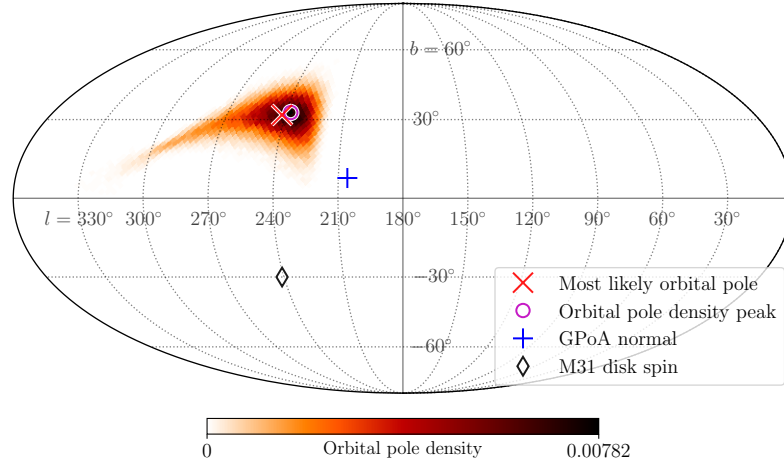


**Figure 9.** Distribution of calculated orbital poles of And III relative to M31 from  $10^5$  Monte-Carlo realizations, in Galactic coordinates. The orbital pole corresponding to the most likely measured position and velocity is shown as a red cross, the peak in the density distribution as a magenta circle. The blue plus sign indicates the normal vector to the GPoA that corresponding to the direction of co-rotation inferred from the line-of-sight velocity coherence, while the black diamond indicates the spin of the galactic disk of M31. See Figure 2 in Pawłowski & Sohn (2021) for equivalent plots for the two other M31 satellites with measured proper motions, NGC 147 and NGC 185.



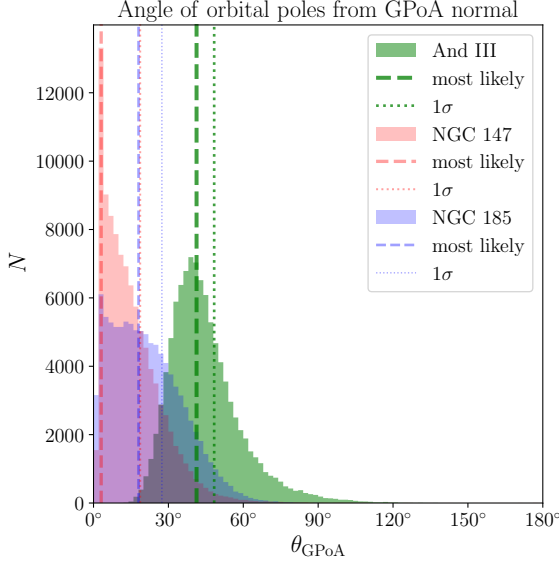


**Figure 10.** Distribution of the angle between the orbital pole of a satellite galaxy and the co-orbiting GPoA normal vector, based on  $10^5$  Monte Carlo samplings from the measurement uncertainties. The dashed lines indicate the angle inferred from the most likely values, while the dotted lines indicate the  $1\sigma$  spreads. Since the spatial position of And III is offset by  $21.5^\circ$  from the GPoA, this is the minimum angular alignment that is geometrically achievable for its orbital pole.

*Facilities: HST, MAST, Gaia*

## REFERENCES

- Anderson, J. 2022, One-Pass HST Photometry with `hst1pass`, Instrument Science Report ACS 2022-02, ,
- Anderson, J., & King, I. R. 1999, *PASP*, 111, 1095
- . 2000, *PASP*, 112, 1360
- . 2003, *PASP*, 115, 113
- Bennet, P., Patel, E., Sohn, S. T., et al. 2023, arXiv e-prints, arXiv:2312.09276
- Casetti-Dinescu, D. I., Baena-Gallé, R., Girard, T. M., Cervantes-Rovira, A., & Todeasa, S. 2024, *PASP*, 136, 054501
- Casetti-Dinescu, D. I., Girard, T. M., Baena-Gallé, R., Martone, M., & Schwendemann, K. 2023, *PASP*, 135, 054501
- Casetti-Dinescu, D. I., Girard, T. M., Kozhurina-Platais, V., et al. 2021, *PASP*, 133, 064505
- Casetti-Dinescu, D. I., Hansen, C. K., Girard, T. M., et al. 2022, *AJ*, 163, 1
- Conn, A. R., Lewis, G. F., Ibata, R. A., et al. 2013, *ApJ*, 766, 120
- Gaia Collaboration, Brown, A. G. A., Vallenari, A., et al. 2021, *A&A*, 649, A1
- Hamaker, H. C. 1978, *Journal of the Royal Statistical Society. Series C (Applied Statistics)*, 27, 76
- Ibata, R. A., Lewis, G. F., Conn, A. R., et al. 2013, *Nature*, 493, 62
- Kirby, E. N., Gilbert, K. M., Escala, I., et al. 2020, *AJ*, 159, 46
- Kozhurina-Platais, V., Borncamp, D., Anderson, J., Grogan, N., & Hack, M. 2015, *ACS/WFC Revised Geometric Distortion for DrizzlePac*, Instrument Science Report ACS/WFC 2015-06, 47 pages, ,
- Kozhurina-Platais, V., Grogan, N., & Sabbi, E. 2018, *Accuracy of the HST Standard Astrometric Catalogs w.r.t. Gaia*, Instrument Science Report ACS 2018-01, 17 pages, ,
- McConnachie, A. W. 2012, *AJ*, 144, 4
- Patel, E., Besla, G., & Sohn, S. T. 2017, *MNRAS*, 464, 3825
- Pawlowski, M. S., & Sohn, S. T. 2021, *ApJ*, 923, 42
- Salomon, J. B., Ibata, R., Reylé, C., et al. 2021, *MNRAS*, 507, 2592
- Savino, A., Weisz, D. R., Skillman, E. D., et al. 2022, *ApJ*, 938, 101

Sohn, S. T., Patel, E., Fardal, M. A., et al. 2020, ApJ, 901,

Taibi, S., Pawlowski, M. S., Khoperskov, S., Steinmetz, M.,  
& Libeskind, N. I. 2024, A&A, 681, A73

43

Warfield, J. T., Kallivayalil, N., Zivick, P., et al. 2023,  
MNRAS, 519, 1189